

Thermal Vision for Soil Assessment in a Multipurpose Environmental Chamber under Martian Conditions towards Robot Navigation

Raúl Castilla-Arquillo^a, Anthony Mandow^a, Carlos J. Pérez-del-Pulgar-Mancebo^a, César Álvarez-Llamas^b, José M. Vadillo^b, and Javier Laserna^b

^a*Department of Automation and Systems Engineering, University of Málaga, Andalucía Tech, 29070 Málaga, Spain,*

^b*UMALASERLAB, Department of Analytical Chemistry, University of Málaga, 29010 Málaga, Spain,*

Abstract

Soil assessment is important for mobile robot planning and navigation on natural and planetary environments. Terramechanic characteristics can be inferred from the thermal behaviour of soils under the influence of sunlight using remote sensors such as Long-Wave Infrared cameras. However, this behaviour is greatly affected by the low atmospheric pressures of planets such as Mars, so practical models are needed to relate robot remote sensing data on Earth to target planetary exploration conditions. This article proposes a general framework based on multipurpose environmental chambers to generate representative diurnal cycle dataset pairs that can be useful to relate the thermal behaviour of a soil on Earth to the corresponding behaviour under planetary pressure conditions using remote sensing. Furthermore, we present an application of the proposed framework to generate datasets using the UMA-Laserlab chamber, which can replicate the atmospheric CO₂ composition of Mars. In particular, we analyze the thermal behaviour of four soil samples of different granularity by comparing replicated Martian surface conditions and their Earth's diurnal cycle equivalent. Results indicate a correlation between granularity and thermal inertia that is consistent with available Mars surface measurements recorded by rovers. The resulting dataset pairs, consisting of representative diurnal cycle thermal images with heater, air, and subsurface temperatures, have been made available for the scientific community.

Keywords: Soil assessment; Thermal inertia; Thermal vision; Multipurpose Environmental Chamber.

1. Introduction

Remote assessment of soils terramechanic characteristics can be crucial for the safety and efficiency of a broad range of tasks related to planetary mobile robot navigation such as odometry, environment mapping or energetic consumption (Wong, 2022). Soil assessment is useful to prevent slipping, skidding and getting entrapped on granular soils, which led to delay and significant mobility difficulties in the Curiosity and Spirit rover missions (Arvidson et al., 2017; Gonzalez and Iagnemma, 2018).

In general, onboard mobile robot sensors such as RGB stereo cameras or 3D laser scanners (Guastella and Muscato, 2020) can be used to infer soil characteristics such as roughness and slope (Nampoothiri et al., 2021). However, these measurements are limited to the surface layer, so relevant subsurface properties for traversability such as soil cohesion or internal friction cannot not be assessed. Alternatively, infrared data has been useful for terrain classification on Mars (Putzig and Mellon, 2007). In this sense, onboard remote sensors such as thermopiles and thermal cameras can provide relevant data to infer subsurface properties from thermal behaviour (Chhaniyara et al., 2012).

Thermopiles are being used in the Curiosity and Perseverance rovers (Gómez-Elvira et al., 2012; Pérez-Izquierdo et al., 2018) to perform on-site measurements of Martian surface thermal behaviour. Furthermore, in the future Martian Moons eXploration (MMX) mission, a rover will be equipped with thermophiles to infer Phobos' composition from its thermal



Figure 1: UMA-Laserlab Mars Environment Chamber used in the experiments.

inertia (Michel et al., 2022). Nevertheless, thermal cameras offer significantly higher resolution, which can be advantageous for assessment and segmentation of heterogeneous soils. For instance, thermal images can be processed to infer soil traversability from measured thermal diffusivity (Cunningham et al., 2015b) or thermal inertia (Cunningham et al., 2015a; Gonzalez et al., 2017).

Thermal imagery is suitable for training neural networks to

classify soils based on their thermal behaviour (Iwashita et al., 2020). In fact, there is a growing interest in image-based machine learning for navigation and terrain classification for planetary rovers (Rothrock et al., 2016; Mandrake et al., 2022). In particular, thermal inertia measurements have been used to train slippage models on rovers (Cunningham et al., 2019) and to improve their autonomy on machine learning systems (Ono et al., 2020). Nonetheless, machine learning approaches are limited by an insufficient amount of representative data, given the difficulty and expense of planetary imaging (Nagle-Mcnaughton et al., 2022; Atha et al., 2022). Besides, the thermal behaviour obtained in experiments on Earth is often different from the behaviour on planets such as Mars, which limits the applicability of the machine learning modelss (Cunningham et al., 2019). Therefore, experimental frameworks are needed to obtain experimental datasets on Earth that are representative of planetary conditions.

The ability to replicate conditions representative of a real scientific mission on other planets is important in experiments for thermal inertia estimations, which are very dependent on pressure (Putzig, 2006). In this sense, Multipurpose Environmental Chambers (MECs) can operate under representative conditions of temperature and pressure found in other planets such as Mars (Vakkada Ramachandran et al., 2020; Wu et al., 2021).

This article addresses on-robot remote sensing for planning and navigation, by proposing a general MEC-based framework to generate representative diurnal cycle dataset pairs. They can be useful to relate the thermal behaviour of a soil on Earth to the corresponding behaviour under planetary pressure conditions using thermal cameras. We analyzed the thermal behaviour of four soil samples of different granularity by comparing replicated Martian surface conditions and their Earth's diurnal cycle equivalent, focusing this analysis on thermal inertia for different type of soils. Results indicate a correlation between granularity and thermal inertia that is consistent with available Mars surface measurements recorded by rovers. Provided framework and its corresponding results are supported by a dataset that was generated using the UMA-Laserlab MEC (see Fig. 1), which can replicate the atmospheric CO₂ composition of Mars. This dataset consists of representative diurnal cycle thermal images with heater, air, and subsurface temperatures for both Earth and Mars conditions, allowing to perform a thermal inertia comparison for different soils. It has been made available for the scientific community.

This article is organized as follows. Section 2 reviews thermal inertia as well as methods to estimate it. Section 3 presents the proposed the MEC-based framework. Section 4 describes the experimental setup. Section 5 introduces the generated dataset and discusses experimental results. Finally, Section 6 offers conclusions and provides an insight on future works.

2. Thermal inertia

This section reviews thermal inertia concepts, the use of the thermal diffusion equation to model the Martian surface thermal behaviour, and two methods to estimate thermal inertia based on surface temperature gradients.

2.1. Definition and pressure dependence

Thermal inertia, I , is defined as follows:

$$I = \sqrt{kpc}, \quad (1)$$

where k is the bulk thermal conductivity, p is the bulk density and c is the soil specific heat capacity. Thermal inertia is the property of a material that affects the resistance of a soil to change its temperature. A higher thermal inertia value means a slower heating of the soil. Thermal conductivity is the parameter which mainly influences thermal inertia. It is affected by three different heat transfer mechanisms (Putzig, 2006):

$$k = k_r + k_c + k_g, \quad (2)$$

where k_r is the transfer across pore spaces; k_c is the conduction between grains contact areas; and k_g is the conduction of the gas which fills the pores between grains. Pressure greatly determines which term acquires the most relevance. Gas conduction (k_g) dominates at pressures between 0.1 mbar and 1000 mbar, where there is a near-linear relationship between particle size and thermal conductivity for granular soils (Presley and Christensen, 1997; Masamune and Smith, 1963). In this case, loose granular soils have lower thermal inertia than compacted rocky soils (Jakosky, 1986a). However, the relationship is not so strong at pressures higher than 1000 mbar. Thus, it is easier to estimate the soils characteristics based on thermal inertia at Martian pressure than at Earth pressure.

2.2. Martian surface behaviour

Martian surface thermal behaviour can be expressed as a boundary condition on the thermal diffusion equation derived from its surface energy budget:

$$G = -I \sqrt{\frac{\pi}{P}} \frac{\partial T}{\partial Z'} \Big|_{Z'=0} = (1-A)R_{sw} - \epsilon\sigma_B T_s^4 + \epsilon R_{lw} - F_{CO_2}, \quad (3)$$

where G is the net heat flux expressed in W/m^2 , A is the albedo, σ_B is the Stefan–Boltzmann constant, R_{sw} is the down-welling shortwave (SW) radiation absorbed from the Sun, R_{lw} is the down-welling longwave (LW) radiation emitted by the atmosphere and the Sun, ϵ is the thermal emissivity, F_{CO_2} is the seasonal CO₂ condensation, P is the period of a diurnal cycle, T_s is the surface temperature, and the term $\frac{\partial T}{\partial Z'} \Big|_{Z'=0}$ is the temperature gradient evaluated at the surface of the terrain, being Z' the distance into the terrain normalized to the thermal skin depth. The sign convention is to use a positive sign when modeling the heating of the terrain and a negative sign when modeling its cooling.

The F_{CO_2} term of Eq. 3 is negligible for Martian surfaces located from equatorial to mid-latitudes that present no frost. Moreover, the down-welling LW radiation is not considered, as previous on-ground measurements have shown it to be an order of magnitude smaller than the rest of terms (Martínez et al., 2014). Thus, the simplified equation for the soil thermal behaviour is:

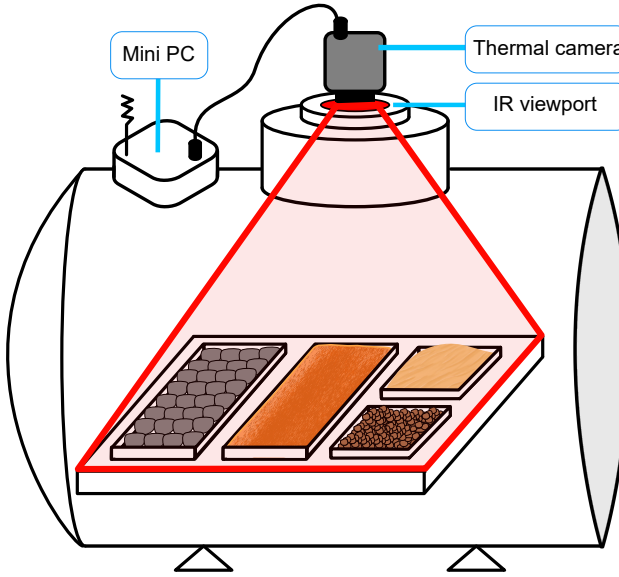


Figure 2: Schematic diagram of the proposed experimental MEC setup.

$$G = -I \sqrt{\frac{\pi}{P}} \frac{\partial T}{\partial Z'} \Big|_{Z'=0} = (1 - A)R_{sw} - \epsilon\sigma_B T_s^4, \quad (4)$$

where the soil thermal behaviour depends on the SW incident Sun's radiation, the thermal inertia and the surface radiative emission.

2.3. Thermal inertia estimation

Thermal inertia represents a complex combination of physical properties that are not directly measurable in practice, so simplified estimations based on surface temperature observations are required (Wang et al., 2010). In this work, we use the Apparent Thermal Inertia (ATI) (Price, 1977) and the method based on daily amplitude of surface soil heat flux and temperature by Wang et al. (2010).

ATI (Price, 1977) is a simple method to estimate the thermal inertia of an outdoors surface subjected to the Sun's heating. This estimation takes into account the diurnal temperature amplitude by measuring the minimum night and maximum day surface temperatures, T_{min} and T_{max} , respectively. The formula to obtain the ATI of a surface is:

$$ATI = \frac{1 - A}{\Delta T_s}, \quad (5)$$

where $\Delta T_s = T_{max} - T_{min}$. The result can be multiplied by a 4186 coefficient to express ATI in thermal inertia units, $tiu \equiv \frac{W_s^{1/2}}{m^2 K}$. Throughout this work, ATI will always be expressed in tiu . Even if ATI is widely used in the literature, this estimation does not consider the surface energy budget, among other limitations (Price, 1985).

The alternative estimation proposed by Wang et al. (2010) considered a sinusoidal approximation of the Earth's net heat flux and surface temperatures for a diurnal period P . The same assumption can be applied to Mars' heat fluxes and temperatures (Martínez et al., 2014). Under this assumption, the thermal inertia of a given soil can be estimated as:

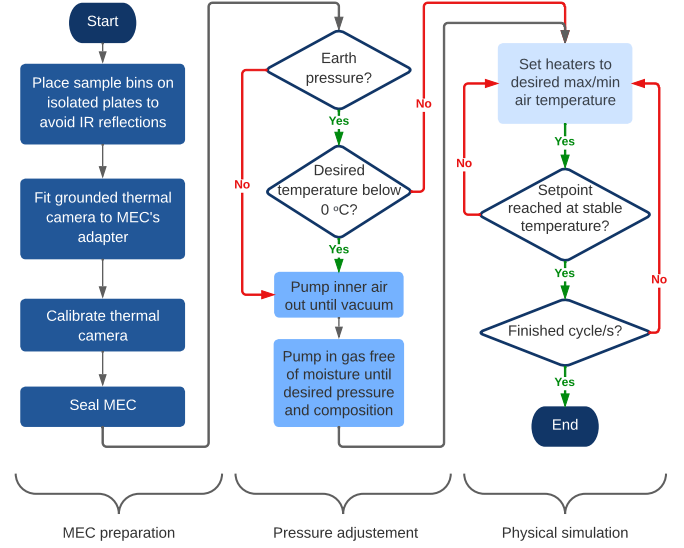


Figure 3: Flow chart of the proposed methodology.

$$I_{sin} = \frac{\Delta G_s}{\Delta T_s \sqrt{2\pi/P}}, \quad (6)$$

where the net heat flux expressed as $\Delta G_s = G_{max} - G_{min}$, being G_{max} and G_{min} the maximum and minimum values of the net heat flux, respectively.

3. MEC-based framework for thermal remote sensing dataset generation

In this section, we propose a general framework for generating representative diurnal cycle thermal behavior datasets of soils under representative pressures. The framework consists of a physical MEC-based configuration (see Fig. 2) and an experimental methodology (see Fig. 3).

The proposed physical configuration (see Fig. 2) allows to perform remote temperature measurements under the extreme conditions produced by the MEC. This configuration consists of an inner plate where the sample bins are placed, an external thermal camera connected to a Mini PC for data collection and an IR viewport. The viewport must allow the infrared range from 8 μ m to 14 μ m to pass through with minimal losses. Furthermore, it must withstand the pressure differential and temperatures reached by the MEC.

The experimental methodology (see Fig. 3) is divided into three sequential tasks: the preparation of the MEC setup; the adjustment of the inner pressure according to the environment to be replicated; and the physical simulation where the actuation profile is defined. In the preparation task, the sample bins are placed on the plate while care is taken to thermally insulate the plate surface, as it can produce IR reflections that can distort the measurements. The thermal camera is placed on the viewport and its housing is connected to ground to avoid the electrostatic charges produced by the MEC pumps. Next, the thermal camera is calibrated to provide precise measurements of the sample bins surfaces and, finally, the MEC gets sealed.

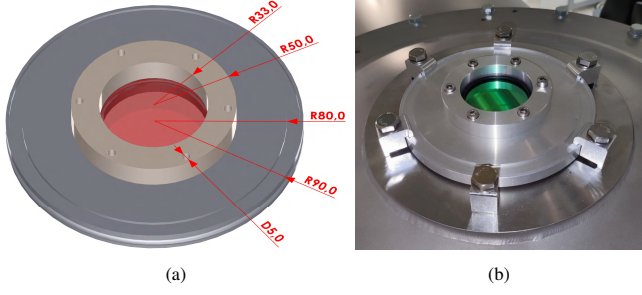


Figure 4: a) 3D model of the viewport adapter (dimensions in millimeters) , b) Customized viewport adapter.

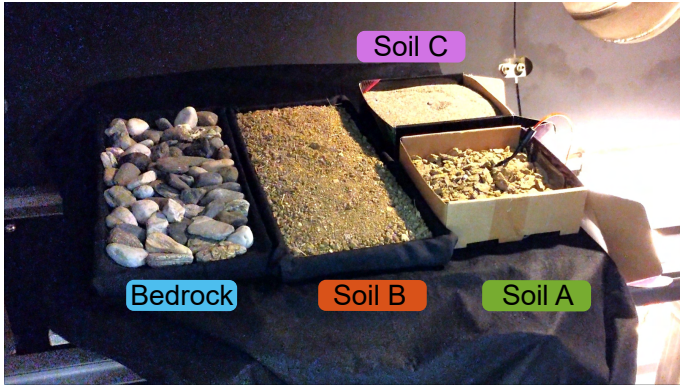


Figure 5: Samples bins of soils of different granularity introduced into the MEC.

In the pressure adjustment task, different procedures have to be performed depending on the pressure and temperature range of the experiments. The simulation can be started if the experiments are planned to be at earth pressure and temperature above 0 °C. Otherwise, the air is pumped out until vacuum and then humidity-free air of the desired composition (i.e., 95 % of CO₂ for Mars) is pumped in. This process prevents the freezing of the air moisture from affecting the MEC internal systems. During the physical simulation part, temperatures are defined for the MEC heaters to obtain sinusoidal soil samples temperatures similar to those obtained in a diurnal cycle in reality.

In the physical simulation, the surface energy budget of each sample bin inside the MEC can be expressed in function of a radiative flux produced by the MEC heaters according to the following equation:

$$G = -I \sqrt{\frac{\pi}{P}} \left. \frac{\partial T}{\partial Z'} \right|_{Z'=0} = \epsilon \sigma_B T_{heater}^4 - \epsilon \sigma_B T_{s_i}^4, \quad (7)$$

where T_{s_i} is the surface mean temperature of each soil and T_{heater} is the MEC heaters temperature. Air natural convection is considered to be negligible as the MEC is an enclosed space with no wind. Inside the MEC, the radiation term $\epsilon \sigma_B T_{heater}^4$ simulates the active Sun heating of the term $(1 - A)R_{sw}$ of Eq. 4.

4. Experimental setup

The framework proposed in Section 3 has been applied to produce representative diurnal cycle datasets for analyzing the thermal behaviour of four soil samples for corresponding Martian and Earth surface conditions. This section presents the integration of hardware components to evaluate the proposed framework as well as the selection of soil samples.

4.1. Equipment

The UMA-Laserlab MEC (see Fig. 1) is a stainless-steel cylinder of 12 m of length and 1.6 m of diameter and viewports on the top and sides (Alvarez-Llamas et al., 2021). It is equipped with an inner spot-gridded thermal jacket or heater which contains a cooling fluid that can reach a temperature in the range of -72 °C to 127 °C, at a rate of 1 °C/min. The air inside can be pumped out until a pressure of 10⁻⁴ mbar is reached and can be replaced by CO₂ to simulate the composition of the atmosphere on Mars. It is equipped with vacuum-compliant thermocouple gauges in the center of its core to measure the air temperature. Additionally, the MEC has a stainless steel plate on rails that allow a payload of up to 70 kg.

The thermal vision camera is a PI-640i by Optris based on uncooled microbolometer technology. It is a 320 g Long-Wave Infrared (LWIR) camera that works in the spectral range of 8 μm to 14 μm, has a resolution of 640x480 pixels and a germanium optic with a field of view of 60° x 45°. It can measure temperatures from -20 °C to 900 °C with a thermal sensitivity of 0.04 °C. We selected this camera due to its high resolution and light weight, making it suitable for mobile and aerial robots. However, this uncooled camera does not provide temperature measurements below -20 °C, which limited the absolute minimum temperature to which the soil samples could be subjected.

The thermal camera was connected to a Mini PC Intel NUC with an Intel Core i5 processor of 1.8GHz and 16GB of RAM running the software Optris PIX Connect. We adjusted the focal length of its optic by using a warm body (i.e., a hand) placed on the plate as a reference. The thermal camera geometric and radiometric calibrations were performed and provided by the manufacturer. The sample bins were placed on the plate perpendicular to the thermal camera at a distance of around 1.3 m to have an undistorted view of their surfaces. The plate surface was covered with insulating cardboards and a thick black fabric to avoid IR reflections of the steel.

We designed and developed a viewport adapter (see Fig. 4) to remotely make measurements from outside the MEC using the thermal camera. It is composed of a IR window that keeps the inside of the MEC sealed while letting the LWIR range from 8 μm to 14 μm radiation pass through. We chose an anti-reflection coated Germanium circular optic model GEW16AR.20 by MKS Instruments due its high mechanical resistance and its ability to withstand abrupt thermal changes. We selected a diameter of 74.9 mm and 5.0 mm of thickness in order to comply with the minimum thickness required to avoid reaching the germanium's fracture strength caused by the pressure differential between the environment and Martian pressure inside the MEC (Yoder Jr, 2005). Furthermore, an aluminium

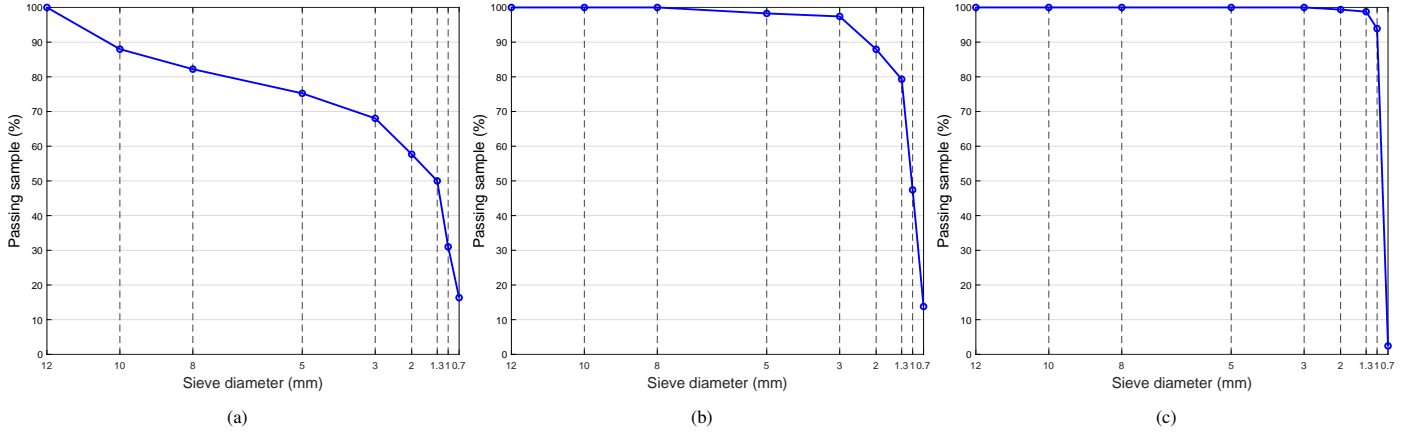


Figure 6: Granularity chart for: a) Soil A, b) Soil B, c) Soil C.

Table 1: Sample bins characteristics. Mean granularity ranges are expressed in mm, density is in g/ml and bin sizes are in cm.

Sample	Granularity	Density	Bin size
Bedrock	40.0 - 50.0	2.94	53 x 23 x 3.5
Soil A	3.0 - 5.0	1.43	22 x 22 x 7
Soil B	1.3 - 2.0	1.40	55 x 23 x 3.5
Soil C	0.7 - 1.0	1.71	22 x 22 x 7

Table 2: Description of the MEC experiments and the soil in which the subsurface thermocouple gauge was located. Pressure is expressed in mbar and the experimental actuation period, P_e , is showed in minutes.

	Experiment	Pressure	Subsurface	P_e
Pair-1	#1 Earth-like	1000	Soil A	296
	#2 Mars-like	8	Soil A	297
Pair-2	#3 Earth-like	1000	Soil C	320
	#4 Mars-like	8	Soil C	360

toroid frame was crafted to place the unclamped Germanium window into the MEC’s upper ISO160K compliant viewports.

4.2. Soil samples

Four sample bins with soils of different characteristics were selected for the experiments (see Fig. 5). Three of the bins contained granular soils and one contained an example of bedrock. Table 1 shows them sorted from highest to lowest mean granularity. We plotted granularity charts of the granular soils (see Fig. 6) by passing them through sieves with grids of different sizes. In terms of homogeneity, Soil C is the most homogeneous, as more than 90 % of its grains have a diameter of 0.7 mm to 1 mm. It is followed by Soil B, whose grains are mostly concentrated on the size of less than 2 mm. Finally, Soil A is classified as the most heterogeneous of the three soils as it consists on a mixture of several grain sizes.

5. Experiments

This section presents the experiments carried out to generate the dataset pairs under Earth’s and Martian conditions using the framework proposed in Section 3. The dataset thermal images

Table 3: Surface temperatures and heat fluxes of the sampled soils at Earth’s and Martian pressures.

		Mean Temp.		Dev.
		T_{init}	ΔT_s	
#1 Earth	Bedrock	24.8	53.3	1.2
	Soil A	24.9	51.1	1.8
	Soil B	25.1	51.6	0.9
	Soil C	24.8	51.4	1.1
#2 Mars	Bedrock	25.0	42.0	1.7
	Soil A	22.7	45.7	2.5
	Soil B	22.4	45.5	0.4
	Soil C	25.0	46.3	1.0
#3 Earth	Bedrock	24.3	48.0	1.3
	Soil A	24.4	45.6	1.8
	Soil B	24.5	45.8	0.8
	Soil C	24.5	46.2	1.1
#4 Mars	Bedrock	25.5	38.3	1.6
	Soil A	24.2	41.3	2.3
	Soil B	24.2	41.2	1.3
	Soil C	24.8	43.0	0.8

were processed to analyze the soils thermal behaviour and to estimate their thermal inertia.

Two pairs of experiments (Pair-1 and Pair-2) were performed in the MEC on the soils defined in Table 1 in order to provide redundant measurements. Table 2 summarizes the main characteristics of each experiment. It was only possible to obtain the subsurface temperature of one of the soils per experiment due to MEC connectivity limitations. The subsurface thermocouple gauge was located a depth of 3 cm in soils A and C for Pair-1 and Pair-2, respectively. The experiment pairs consist of Earth representative (1000 mbar) (#1 and #3) and Mars representative (8 mbar) (#2 and #4) pressures. Besides, or the Mars-like experiments, air with Mars’ Carbon Dioxide (CO₂) atmospheric composition of 95 % was introduced into the MEC. On-site near-equatorial environmental measurements performed by Mars Science Laboratory (MSL) showed mean daily air temperatures of around -50°C with approximate amplitudes of 60°C (Martínez et al., 2017). Thus, sinusoidal temperatures of similar amplitude were simulated in diurnal cycles of experi-

mental actuation period P_e by manual input of constant heating and cooling setpoints for MEC actuation.

5.1. Soils thermal behaviour

Soil surface temperatures were measured by means of the Optris PI-640i thermal camera. The thermal remote sensing was done as realistically as possible to an actual on-robot implementation, so no prior knowledge of the soils was assumed. Thus, emissivity (ϵ) was considered to be unitary and the albedo (A) to be zero for all the soils, according to Kirchhoff's law: $1 = A + \epsilon$ (Vollmer, 2021). Polygonal areas delimiting each soil were defined in the acquired thermal images, where the pixels showing the thermocouple gauge were removed so as not to affect the temperature measurements.

Figures 7-10 show the diurnal cycle temperatures for all soil types from experiments #1-#4, respectively. Besides, Figs. 11 and 12 present surface and subsurface temperature readings for soil A (experiments #1 and #2) and soil C (experiments #3 and #4), respectively. All figures show the heater, setpoint and air temperatures. The transient is assumed to end when an inflection point is reached in the upwards heater temperature response. Moreover, Table 3 presents soil surface mean temperatures for the pixels in the corresponding polygonal area together with standard deviations for the four experiments. In the table, $\Delta T_s = T_{max} - T_{init}$, being T_{max} the maximum mean temperature and T_{init} the mean temperature when actuation starts. T_{tran} specifies the standard deviation temperature of each soil when the actuation transient ends. Net heat fluxes were computed by applying the surface energy budget equation of each sample bin inside the MEC (see Eq. 7) using the soils mean temperatures and the MEC heater temperatures obtained during the experiments. $\Delta G_s = G_{max} - G_{init}$, being G_{max} the maximum net heat flux and G_{init} the net heat flux when actuation starts.

First, we compare the surface mean temperatures of pair-1 (Figs. 7a and 8a). The graphs show that only the bedrock is distinguishable at terrestrial pressure as all the granular soils present similar temperatures. On the other hand, at Martian pressure, the soils can be classified into three groups based on their temperature during the MEC heating; from highest to lowest: (1) Soil C; (2) Soil A and B; and (3) bedrock. Besides, both graphs show a slight temporal delay of the bedrock temperature over the rest of soils. The same analysis can be applied to the graphs of pair-2 (Figs. 9a and 10a).

Next, we compare the soils standard deviation curves of pair-1 (Figs. 7b and 8b). All the soils can be classified using the standard deviation of the surface temperatures at both Earth's and Mars' pressures from the start of the actuation until the transient ends. This behaviour can be due to their granularity: heterogeneous soils (e.g., Soil A) show higher standard deviation temperatures than more homogeneous soils (e.g., Soil C). This behaviour becomes more evident in the Martian case. A similar analysis can be applied to the graphs of pair-2 (Figs. 9b and 10b).

Finally, we compare the mean surface value with the subsurface temperatures of Soil A in pair-1 (Figs. 11a and 11b). In this case, the maximum difference between the surface and subsurface temperature are 11.6 °C and 14.7 °C at Earth's and Mar's

Table 4: Estimated values of thermal inertia for each soil.

		Bedrock	Soil A	Soil B	Soil C
I_{sin}	#1 Earth	309	322	312	314
	#2 Mars	522	411	411	370
	#3 Earth	311	323	320	310
	#4 Mars	548	431	431	379
ATI	#1 Earth	79	82	81	81
	#2 Mars	100	92	92	90
	#3 Earth	87	92	91	91
	#4 Mars	109	101	102	97

pressure, respectively; which constitutes an increase of 26.72%. As for Soil C in pair-2 (Figs. 12a and 12b), for Earth, the maximum difference is 14.4 °C, whereas for Mars-like it is 24.4 °C; which is a 69.44% increase. Based on this data, we can conclude that the thermal inertia of both soils increases when the pressure decreases, as it gets more difficult for the heat to be transmitted vertically.

5.2. Thermal inertia estimation

We computed estimations of each soil thermal inertia based on the ΔT_s , ΔG_s and P_e values obtained during the experiments. For comparison purposes, we used both the ATI (Eq. 5) and the sinusoidal estimation, I_{sin} (Eq. 6). The estimated values are shown in Table 4.

Regarding the sinusoidal estimations, I_{sin} , it is observed that thermal inertia increases when pressure decreases. Thus, soils are easier to classify at Martian pressure than at Earth's pressure. Soils with larger particle sizes, e.g., Bedrock, have higher thermal inertia; on the other hand, soils with smaller particles, e.g., Soil C, show lower thermal inertia. The estimated values under Martian conditions of the bedrock are consistent with the on-site thermal inertia obtained by Curiosity for bedrock-dominated surfaces ($\sim 350 - 550$ tiu) (Vasavada et al., 2017). As for Soil C, its estimated thermal inertia is similar to surfaces of around 1 mm mean particle size also derived from Curiosity's data ($\sim 265 - 375$ tiu) (Hamilton et al., 2014). On the other hand, soils A and B present similar thermal inertia despite having different particle size. In this case, Jakosky (1986b) argued that soils with particle sizes from 1 mm to a few centimeters have a constant thermal inertia of ~ 420 tiu. In conclusion, at Earth's pressure, the mean relative difference of the highest inertia soil compared with the lowest inertia soil is 4.20%; while at Martian pressure the difference is 42.84%.

As for the ATI estimations, even though the relative differences between soils are consistent, they do not display a significant increase of their absolute values when the pressure decreases. This is mainly due to the fact that ATI does not consider the soils heat fluxes inside the MEC. Thus, thermal inertia estimations using the ATI equation are not adequate enough for this kind of experiments.

5.3. Dataset

During the experiments, we collected a total of 9225 radiometric images. Each image recorded by the thermal camera

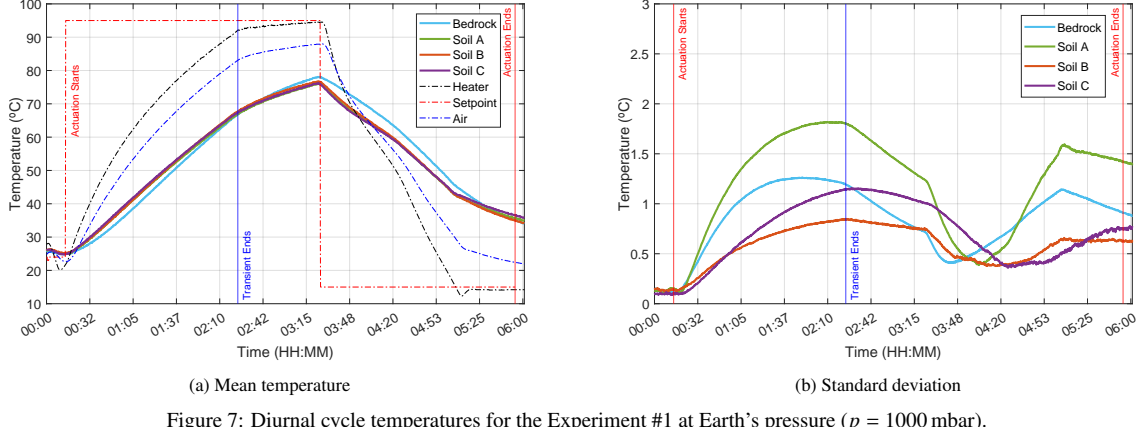


Figure 7: Diurnal cycle temperatures for the Experiment #1 at Earth's pressure ($p = 1000$ mbar).

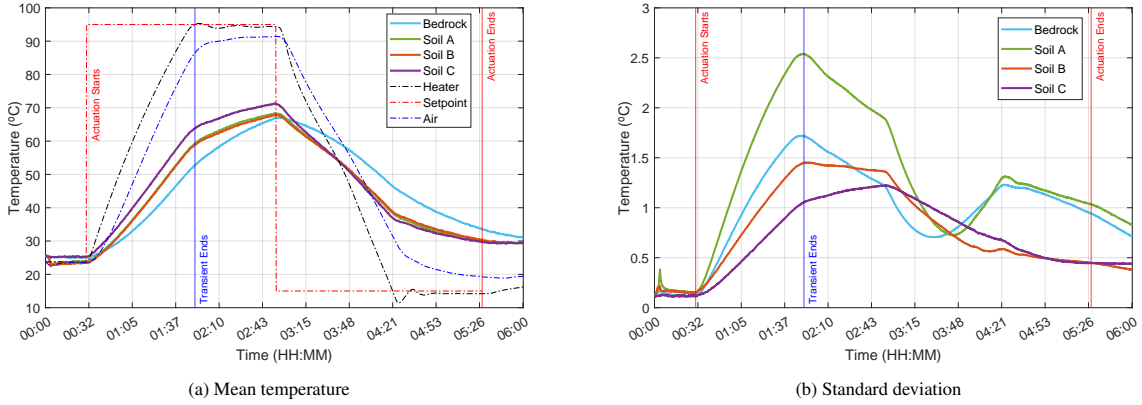


Figure 8: Diurnal cycle temperatures for the Experiment #2 at Martian pressure ($p = 8$ mbar).

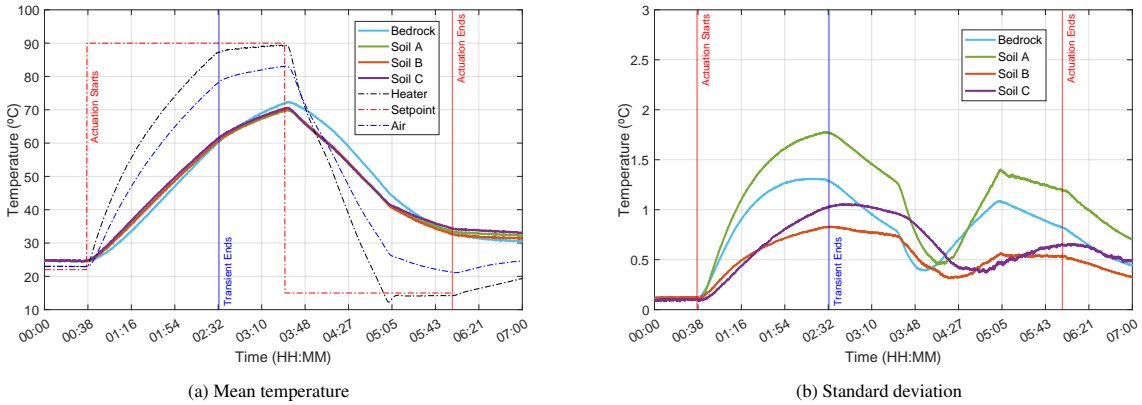


Figure 9: Diurnal cycle temperatures for the Experiment #3 at Earth's pressure ($p = 1000$ mbar).

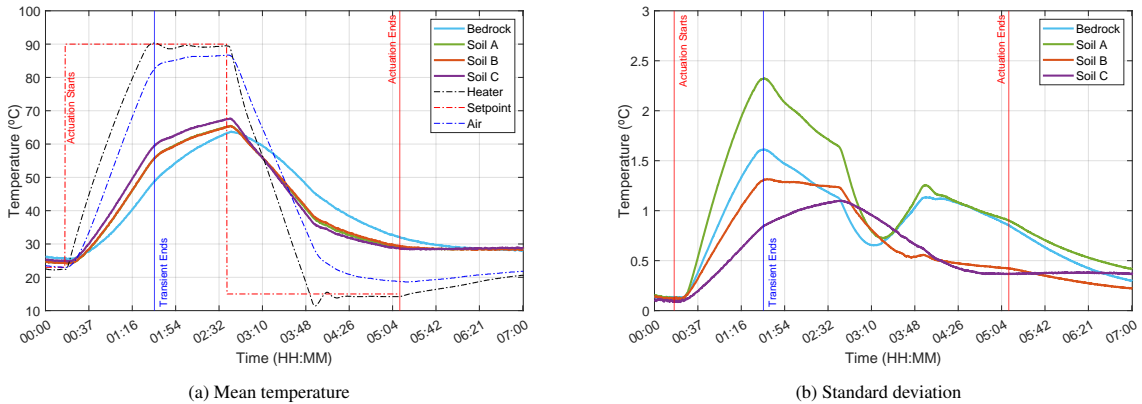
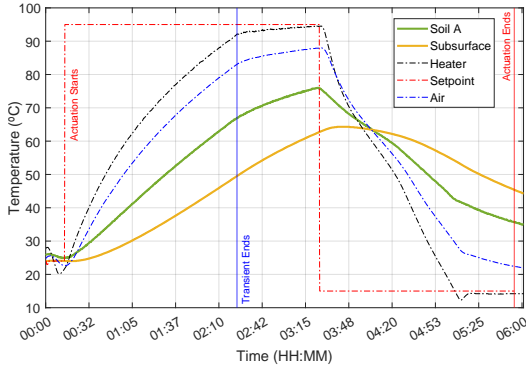
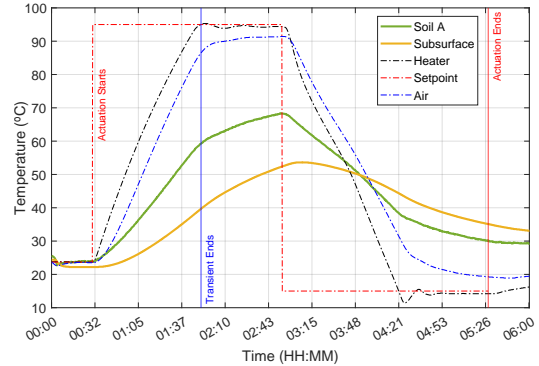


Figure 10: Diurnal cycle temperatures for the Experiment #4 at Martian pressure ($p = 8$ mbar).

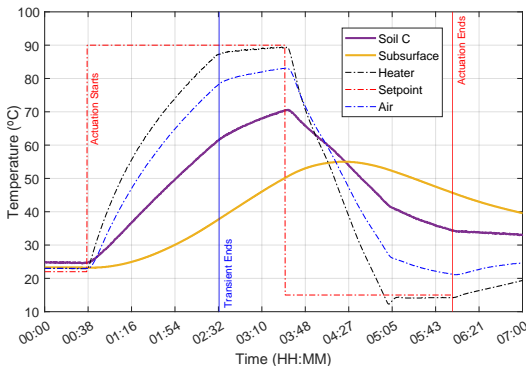


(a) Earth's pressure (Experiment #1)

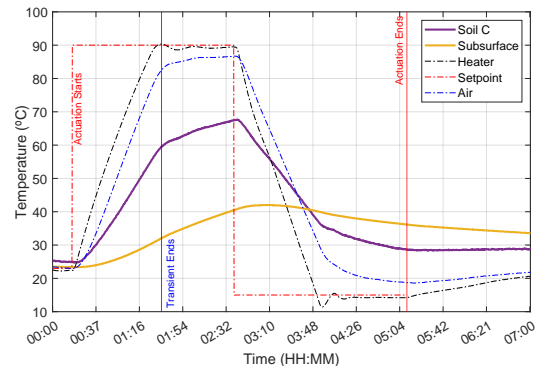


(b) Martian pressure (Experiment #2)

Figure 11: Diurnal cycle surface and subsurface temperatures of Soil A.



(a) Earth's pressure (Experiment #3)



(b) Martian pressure (Experiment #4)

Figure 12: Diurnal cycle surface and subsurface temperatures of Soil C.

was saved as a plain text 640 x 480 matrix with each cell containing the temperature in degrees Celsius. Snapshots of the thermal images were processed to facilitate direct viewing. An example of one of these snapshot is shown in Fig. 13 Finally, spreadsheets were generated with the heaters, air, and subsurface temperatures recorded by the thermocouples. To the authors' knowledge, no similar dataset exists in the literature. A public dataset with the recorded data can be found at Zenodo¹.

6. Conclusions and future work

This article proposes a general framework to generate remotely measured diurnal cycle dataset pairs on soils subjected to planetary exploration conditions using MECs. A dataset was generated on different soils from the experiments carried out in the UMA-Laserlab MEC under Earth's and Mars' conditions. To the authors' knowledge, no similar dataset exists in the literature. The obtained data was processed to estimate the thermal inertia values of the soils. These values were compared with real on-site estimations performed by rovers of Mars, showing that our framework is capable of physically simulating the soil thermal behaviour under Mars' conditions.

Based on the analysis of the experiments carried out in this paper, we conclude that thermal vision cameras can be useful to

remotely assess soils under Martian pressures. This is equally true under Earth's conditions: although relative thermal inertia are less dependant on soils characteristics, measurements of surfaces mean temperatures and standard deviations can potentially provide information about soils characteristics. Thus, soil classification algorithms based on thermal vision that work on Earth will perform much better on Mars. Additionally, the generation of diurnal cycle dataset pairs enables the research of new terrain classification techniques using vision cameras.

Future work will be focused on developing on-robot terrain classifiers based on machine learning algorithms trained with thermal images. Furthermore, we will develop multimodal sensors combining thermal vision together with color and depth information to enhance the autonomous assessment of unstructured environments. Studies can also be focused on implementing this kind of algorithms on drones as NASA is planning to use helicopters on future Mars missions.

Declaration of Competing Interest

The authors declare that they have no known competing financial interests or personal relationships that could have appeared to influence the work reported in this paper.

¹<http://doi.org/10.5281/zenodo.7750148>

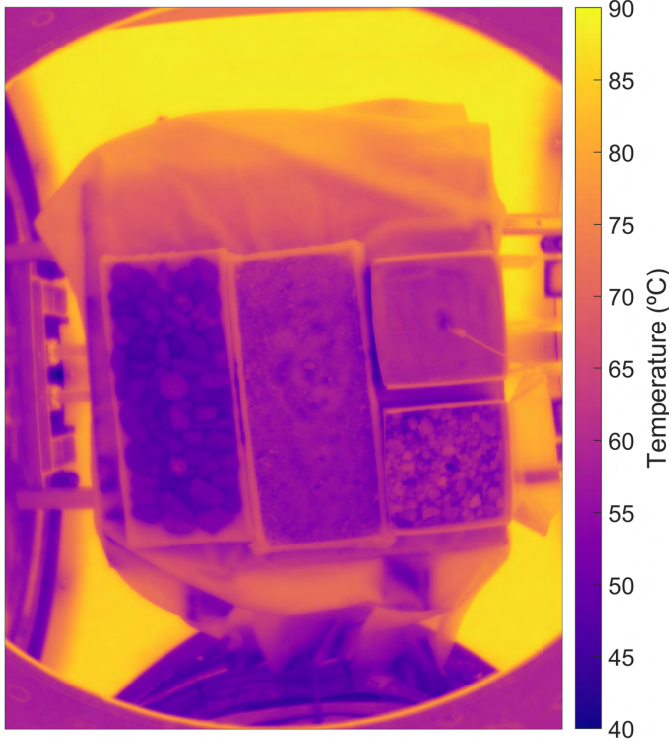


Figure 13: Example of a thermal image of the sample bins during the experiments.

Acknowledgements

This work was supported by the Andalusian Regional Government under the project entitled "Intelligent Multimodal Sensor for Identification of Terramechanic Characteristics in Off-Road Vehicles (IMSITER)" under grant agreement P18-RT-991.

References

Alvarez-Llamas, C., Purohit, P., Moros, J., Lucena, P., Laserna, J., Vadillo, J., 2021. A multipurpose thermal vacuum chamber for planetary research compatible with stand-off laser spectroscopies, in: 52nd Lunar and Planetary Science Conference, p. 2330.

Arvidson, R.E., Iagnemma, K.D., Maimone, M., Fraeman, A.A., Zhou, F., Heverly, M.C., Bellutta, P., Rubin, D., Stein, N.T., Grotzinger, J.P., et al., 2017. Mars science laboratory curiosity rover megaripple crossings up to sol 710 in gale crater. *Journal of Field Robotics* 34, 495–518.

Atha, D., Swan, R.M., Didier, A., Hasnain, Z., Ono, M., 2022. Multi-mission terrain classifier for safe rover navigation and automated science, in: IEEE Aerospace Conference Proceedings.

Chhaniyara, S., Brunskill, C., Yeomans, B., Matthews, M., Saaj, C., Ransom, S., Richter, L., 2012. Terrain trafficability analysis and soil mechanical property identification for planetary rovers: A survey. *Journal of Terramechanics* 49, 115–128.

Cunningham, C., Nesnas, I., Whittaker, W.L., 2015a. Terrain traversability prediction by imaging thermal transients, in: 2015 IEEE International Conference on Robotics and Automation (ICRA), IEEE. pp. 3947–3952.

Cunningham, C., Nesnas, I.A., Whittaker, W.L., 2019. Improving slip prediction on mars using thermal inertia measurements. *Autonomous Robots* 43, 503–521.

Cunningham, C., Wong, U., Peterson, K.M., Whittaker, W.L.R., 2015b. Predicting terrain traversability from thermal diffusivity, in: Field and Service Robotics: Results of the 9th International Conference, Springer. pp. 61–74.

Gómez-Elvira, J., Armiens, C., Castañer, L., Domínguez, M., Genzer, M., Gómez, F., Haberle, R., Harri, A.M., Jiménez, V., Kahapää, H., et al., 2012. Rems: The environmental sensor suite for the mars science laboratory rover. *Space science reviews* 170, 583–640.

Gonzalez, R., Iagnemma, K., 2018. Slippage estimation and compensation for planetary exploration rovers. state of the art and future challenges. *Journal of Field Robotics* 35, 564–577.

Gonzalez, R., Lopez, A., Iagnemma, K., 2017. Thermal vision, moisture content, and vegetation in the context of off-road mobile robots. *Journal of Terramechanics* 70, 35–48.

Guastella, D.C., Muscato, G., 2020. Learning-based methods of perception and navigation for ground vehicles in unstructured environments: A review. *Sensors* 21, 73.

Hamilton, V.E., Vasavada, A.R., Sebastián, E., de la Torre Juárez, M., Ramos, M., Armiens, C., Arvidson, R.E., Carrasco, I., Christensen, P.R., De Pablo, M.A., et al., 2014. Observations and preliminary science results from the first 100 sols of msl rover environmental monitoring station ground temperature sensor measurements at gale crater. *Journal of Geophysical Research: Planets* 119, 745–770.

Iwashita, Y., Nakashima, K., Gatto, J., Higa, S., Stoica, A., Khoo, N., Kurozume, R., 2020. Virtual ir sensing for planetary rovers: Improved terrain classification and thermal inertia estimation. *IEEE Robotics and Automation Letters* 5, 6302–6309.

Jakosky, B.M., 1986a. On the thermal properties of martian fines. *Icarus* 66, 117–124.

Jakosky, B.M., 1986b. On the thermal properties of martian fines. *Icarus* 66, 117–124.

Mandrake, L., Doran, G., Goel, A., Ono, H., Amini, R., Feather, M.S., Fesq, L., Slingerland, P., Perry, L., Bycroft, B., Kaufman, J., 2022. Space applications of a trusted ai framework: Experiences and lessons learned.

Martínez, G., Newman, C., De Vicente-Retortillo, A., Fischer, E., Renno, N., Richardson, M., Fairén, A., Genzer, M., Guzewich, S., Haberle, R., et al., 2017. The modern near-surface martian climate: a review of in-situ meteorological data from viking to curiosity. *Space Science Reviews* 212, 295–338.

Martínez, G., Rennó, N., Fischer, E., Borlina, C., Hallet, B., De La Torre Juárez, M., Vasavada, A., Ramos, M., Hamilton, V., Gómez-Elvira, J., et al., 2014. Surface energy budget and thermal inertia at gale crater: Calculations from ground-based measurements. *Journal of Geophysical Research: Planets* 119, 1822–1838.

Masamune, S., Smith, J., 1963. Thermal conductivity of beds of spherical particles. *Industrial & Engineering Chemistry Fundamentals* 2, 136–143.

Michel, P., Ulamec, S., Böttger, U., Grott, M., Murdoch, N., Vernazza, P., Sunday, C., Zhang, Y., Valette, R., Castellani, R., et al., 2022. The mmx rover: performing in situ surface investigations on phobos. *Earth, Planets and Space* 74, 1–14.

Nagle-Menaughton, T.P., Scuderi, L.A., Erickson, N., 2022. Squeezing data from a rock: Machine learning for "M"artian science. *Geosciences* 12.

Nampoothiri, M.H., Vinayakumar, B., Sunny, Y., Antony, R., 2021. Recent developments in terrain identification, classification, parameter estimation for the navigation of autonomous robots. *SN Applied Sciences* 3, 1–14.

Ono, M., Rothrock, B., Otsu, K., Higa, S., Iwashita, Y., Didier, A., Islam, T., Laporte, C., Sun, V., Stack, K., et al., 2020. MAARS: Machine learning-based analytics for automated rover systems, in: 2020 IEEE aerospace conference, IEEE. pp. 1–17.

Pérez-Izquierdo, J., Sebastián, E., Martínez, G.M., Bravo, A., Ramos, M., Manfredi, J.A.R., 2018. The thermal infrared sensor (TIRS) of the mars environmental dynamics analyzer (MEDA) instrument onboard mars 2020, a general description and performance analysis. *Measurement* 122, 432–442.

Presley, M.A., Christensen, P.R., 1997. The effect of bulk density and particle size sorting on the thermal conductivity of particulate materials under martian atmospheric pressures. *Journal of Geophysical Research: Planets* 102, 9221–9229.

Price, J.C., 1977. Thermal inertia mapping: A new view of the earth. *Journal of Geophysical Research* 82, 2582–2590.

Price, J.C., 1985. On the analysis of thermal infrared imagery: The limited utility of apparent thermal inertia. *Remote sensing of Environment* 18, 59–73.

Putzig, N.E., 2006. Thermal inertia and surface heterogeneity on Mars. University of Colorado at Boulder.

Putzig, N.E., Mellon, M.T., 2007. Apparent thermal inertia and the surface heterogeneity of mars. *Icarus* 191, 68–94.

Rothrock, B., Papon, J., Kennedy, R., Ono, M., Heverly, M., Cunningham, C., 2016. SPOC: deep learning-based terrain classification for Mars rover missions, in: AIAA Space and Astronautics Forum and Exposition, SPACE 2016.

Vakkada Ramachandran, A., Nazarius, M.I., Mathanlal, T., Zorzano, M.P., Martín-Torres, J., 2020. Space environmental chamber for planetary studies. *Sensors* 20, 3996.

Vasavada, A.R., Piqueux, S., Lewis, K.W., Lemmon, M.T., Smith, M.D., 2017. Thermophysical properties along curiosity's traverse in gale crater, mars, derived from the remss ground temperature sensor. *Icarus* 284, 372–386.

Vollmer, M., 2021. Infrared thermal imaging. Springer.

Wang, J., Bras, R., Sivandran, G., Knox, R., 2010. A simple method for the estimation of thermal inertia. *Geophysical Research Letters* 37.

Wong, J.Y., 2022. Theory of ground vehicles. John Wiley & Sons.

Wu, Z., Ling, Z., Zhang, J., Fu, X., Liu, C., Xin, Y., Li, B., Qiao, L., 2021. A mars environment chamber coupled with multiple in situ spectral sensors for mars exploration. *Sensors* 21, 2519.

Yoder Jr, P.R., 2005. Opto-mechanical systems design. CRC press.